Atomically Dispersed Iridium on MgO(111) Nanosheets Catalyze Benzene-Ethylene Coupling towards Styrene

Pengxin Liu[1*], Xing Huang[2], Deni Mance[1], Christophe Copéret[1*]

[1]Department of Chemistry and Applied Biosciences, ETH Zürich, Zürich, Switzerland.
[2]The Scientific Center for Optical and Electron Microscopy (ScopeM), ETH Zürich, Zürich, Switzerland.
E-mail: pengxin@ethz.ch; ccoperet@ethz.ch

1   **Abstract**

2   Single atom catalysis has been recently recognized as an efficient utilization of metals in heterogeneous
3   catalysis with the possibility to engender unusual reactivity. Yet, despite the observation of single atoms,
4   controlling the uniformity in the coordination structures of supported species and understanding the
5   structure-property relationships remains a grand challenge due to the surface structural complexity of the
6   supports. Here, we combined the use of single-crystalline MgO(111) 2D nanosheets with surface
7   organometallic chemistry to generate highly dispersed Ir(III) sites. The MgO(111) surfaces enable the
8   formation of isolated Ir(III) single-sites stabilized by three 3-coordinated surface -O(H) anions at low
9   loading (0.1 $\%_{wt}$) as well as Ir pairs and trimers at higher loading (1 $\%_{wt}$). These materials show unique
10 catalytic properties and enable the coupling of benzene and ethylene into styrene, in contrast to the
11 expected ethylbenzene, formed with the corresponding Ir-based homogeneous catalysts or with
12 atomically dispersed Ir on MgO nanoparticles.

13

14 Atomically dispersed metal catalysts (also referred to as single-site or single atom catalysts)[1,2] have
15 received increasing attention in recent years due to their unique structures and performances. The
16 maximized atom exposure not only improves the atom efficiency in terms of utilization of precious metals,
17 but it also provides unconventional geometric and electronic structures to the active sites, endowing
18 atomically dispersed metal catalysts with unique catalytic properties.[3-11]

19 While extensive efforts have been devoted to developing synthetic methods and describing catalytic
20 behaviors, understanding the structure-function relationship on an atomic level still remains a challenge.
21 The difficulty lies in controlling and characterizing the coordination environment around single atoms that
22 should largely determine the overall catalytic performance.[12-14] The challenges arise from several factors:
23 (1) the inherent heterogeneity of support surfaces associated with binding sites (corners, edges and faces),
24 defects (vacancies, terraces, grain boundaries etc.) and amorphous structures (hydrated layers,
25 amorphous supports etc.),[15-17] (2) the complexity of surface chemistry using conventional preparation
26 methods, where dissolution/precipitation events take place upon deposition of the active centers, (3)
27 dynamic behavior of single atoms[18-21] and (4) the lack of available characterization techniques to probe
28 the atoms (mostly C/N/O) directly bonded to the single atoms.[22-24] Overall, although atomically dispersed
29 catalysts are usually referred to as analogs of well-defined homogenous catalysts,[25,26] the interaction
30 between ligands (supports) and the metal centers are far less understood by comparison with what can
31 be achieved in coordination and organometallic chemistry.

32 To tackle these problems, we reasoned that well-defined 2D nanomaterials, here the single-crystalline
33 MgO(111) nanosheets,[27] could serve as an ideal support that offers high-surface area, strong binding sites

34 and most importantly, uniform coordination environment. Combined with surface organometallic
35 chemistry (SOMC), that allow the selective incorporation of active centers by grafting well-defined
36 molecular precursors,[28-30] the proposed approach should provide an ideal way to generate uniform
37 atomically dispersed metal centers on the well-defined support. We first selected iridium due to its
38 reactivity towards the selective activation of C-H bonds,[31,32] its catalytically activity towards the arylation
39 of olefins with O-donor ligands,[33,34] as well as its stability in reductive environment at elevated
40 temperature.[35] Herein, we report the synthesis and the characterization of atomically dispersed Ir over
41 MgO(111) nanosheets with molecular-level precision via SOMC approach. We find an unexpected catalytic
42 activity in the coupling of ethylene and benzene to yield styrene, contrasting with the known arylation
43 activity of the corresponding homogeneous system or supported system on MgO nanoparticles yielding
44 ethylbenzene under similar conditions, showing the uniqueness of iridium single atoms dispersed on
45 MgO(111).

46 **Results and Discussion**

47 Single-crystalline MgO(111) nanosheets were contacted with Ir(COD)(acac) (COD = cyclooctadiene; acac =
48 acetylacetonate) in pentane for 3 hours. The consumption of Mg-OH (3573 cm^{-1}), together with the
49 appearance of bridging -O-H (3513 cm^{-1}, 3374 cm^{-1}) and C-H (3080 - 2840 cm^{-1}) stretches according to
50 infrared (IR) spectroscopy (Figure 1b, Figure S1) supports an anchoring process via grafting (Figure 1a).
51 Upon grafting, the C=O stretch of the acac ligands shifted from 1565 cm^{-1} to 1618 cm^{-1}, which is consistent
52 with the transfer of the ligand from iridium to magnesium. In fact, similar IR signatures at 1620 cm^{-1} for C-
53 O stretch and 3513 cm^{-1} for bridging -O-H are obtained upon reacting acetylacetone with MgO (Figure S2)
54 and $Ir(C_2H_4)_2$(acac) with MgO.[36] Analysis of the supernatant showed that all Ir(COD)(acac) (ca. 0.1
55 equivalent to surface -OH groups, 2 Mg-OH/nm^2) precursors are grafted, thus providing a material with 1
56 wt% Ir loading as confirmed by elemental analysis (ca. 0.2 Ir /nm^2). We also prepare a material at 0.1wt%
57 Ir loading, which shows similar spectroscopic characteristics (vide infra).

58 We first investigated the nature of the Ir sites by CO adsorption combined with IR spectroscopy and X-ray
59 absorption spectroscopy (XAS). IR of the grafted sample contacted with CO (Figure S3) shows two CO
60 bands at 2033 cm^{-1} and 1953 cm^{-1} upon exposure to 10 μbar CO at 25 °C, corresponding to symmetric and
61 antisymmetric C−O vibrations bound to Ir. Treatment under higher concentration of CO led to complete
62 removal of COD ligands and reduction of Ir(I) to Ir(0) (Figure S4).[37,38] Similar C−O vibrations bands (2043
63 cm^{-1} and 1965 cm^{-1}) associated with Ir gem-dicarbonyls are observed upon reacting $Ir(CO)_2$(acac) with
64 MgO support (Figure S3); the slightly redshifted v_{CO} values and band broadening are likely due to dipole-
65 dipole interactions [also observed when high dose CO adsorbed on Ir(COD)(acac)/MgO, Figure S4]. The
66 presence of a gem-dicarbonyl Ir surface species was confirmed by isotope labeling: upon adsorption of
67 1:1 ^{12}CO/^{13}CO, the IR spectrum showed 6 bands corresponding to symmetric and antisymmetric vibrations
68 of Ir(^{12}CO)(^{12}CO), Ir(^{12}CO)(^{13}CO) and Ir(^{13}CO)(^{13}CO) structures (Figure S5).[39,40] The presence of iridium gem-
69 dicarbonyl confirms the presence of isolated Ir sites and indicates the lability of the COD ligand. The Ir LIII-
70 edge X-ray absorption near-edge structure (XANES) spectrum showed a slightly shifted white line
71 comparing to Ir(COD)(acac), which indicates a change in the coordination environment (Figure S6). The
72 Fourier-transform extended X-ray absorption fine structure (FT-EXAFS) spectrum could be adequately
73 fitted using a structure close to the molecular precursor, showing 2 oxygen atoms from the support
74 replaced acac$^-$ ligands, that is consistent with the proposed structure in Figure 1a. The Ir-O scattering path
75 was shortened from 2.03 ± 0.01 Å in the free complex to 1.94 ± 0.01 Å in the grafted ones. Ir-C scattering
76 path at 2.09 ± 0.01 Å showed no apparent changes after grafting (2.10 ± 0.01 Å) (Figure 1c, Table S1).
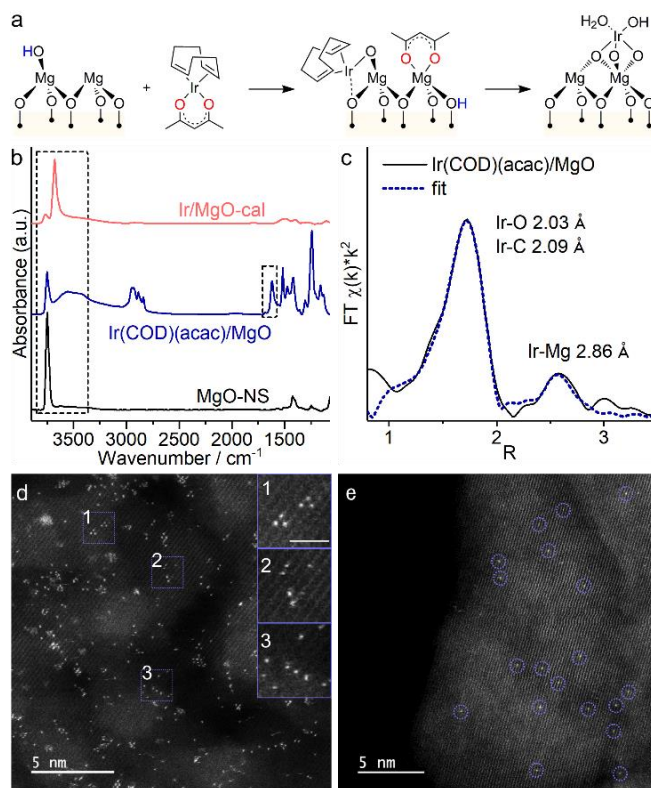
Figure 1. Materials preparation and characterization (a) schematic procedure for grafting of Ir(COD)(acac) on MgO-NS, followed by calcination to form Ir/MgO catalysts. (b) IR characterization of the support, the grafted and the calcined materials. (c) IR characterization of the grafted material with CO adsorbed as probe molecules, in comparison to Ir(CO)$_2$(acac)/MgO. Representative ADF-STEM images of (d) 1 wt% and (e) 0.1 wt% Ir/MgO-cal catalysts.

Subsequent calcination of the grafted material in synthetic air removed all the organic ligands and led to the appearance of a new band at 3680 cm^{-1} in IR, which is assigned to -OH, likely at Ir-O(H)-Mg sites. No diffraction associated with metallic Ir or IrO$_x$ particles was observed by powder X-ray diffraction (XRD), consistent with the formation of highly dispersed Ir sites (Figure S7). Annular dark-field scanning transmission electron microscope (ADF-STEM) images of 1 wt% and 0.1 wt% Ir/MgO-cal samples show no presence of Ir nanoparticle (Figure 1d, e, Figure S8, S9). In contrast, for both materials, highly dispersed Ir atoms are found at the surface of the material; close look reveals that they exclusively sit on the bright Mg atom sites, which indicates that Ir atoms likely locate at positions similar to Mg cations. For 1 wt% Ir/MgO-cal, Ir was found as monomers, dimers, trimers as well as small clusters. 68 % of all Ir atoms (86 % of Ir assemblies) are single atoms based on statistics of over 800 counts (Figure S8). Interestingly, all the trimer sites appear to be structurally similar, with a distance between adjacent Ir atoms of 3.0 Å. Such a value was then used to distinguish dimers from two neighboring monomers by measuring the spacing between two atoms. The measured Ir-Ir distance was identical to Mg-Mg distance on MgO(111) projection (2.98 Å), which nicely demonstrates that Ir has the same coordination structure as Mg cations on MgO(111). Hence, the trimer sites are likely linked by an μ^3-oxygen anion, while two Ir atoms are likely bound by a μ^2-oxygen in dimers. For comparison, Ir-Ir distance in metallic Ir (2.71 Å) is much shorter while this in IrO$_2$ is longer (3.14 Å) than observed here.

100   For the 0.1 wt% sample, all Ir species are uniformly dispersed as isolated single atoms. For these
101   monomers, the most possible binding structure is that three three-fold coordinated O anions (O_{3c}^{2-}) or -
102   OH groups ($-OH_{3c}$) on the flat support surface stabilized one Ir atom, considering the prepared MgO(111)
103   nanosheets is terminated by O_{3c}^{2-}. Such a structure is also assigned to be the most stable one on edge
104   sites of MgO(100) nanocubes.[36] It is likely that the site-isolated Ir atoms on 0.1 wt% sample adapt identical
105   coordination structures. Such a uniform structure is only possible due to the single-crystalline 2D support
106   with well-defined surfaces, thus minimizing the surface heterogeneity. The observed Ir atoms by
107   microscopy are more likely to be adatoms supported on the surface (Figure 1a) rather than embedded in
108   the lattice, because MgO has extremely low atom mobility due to ionic bonding.[41]
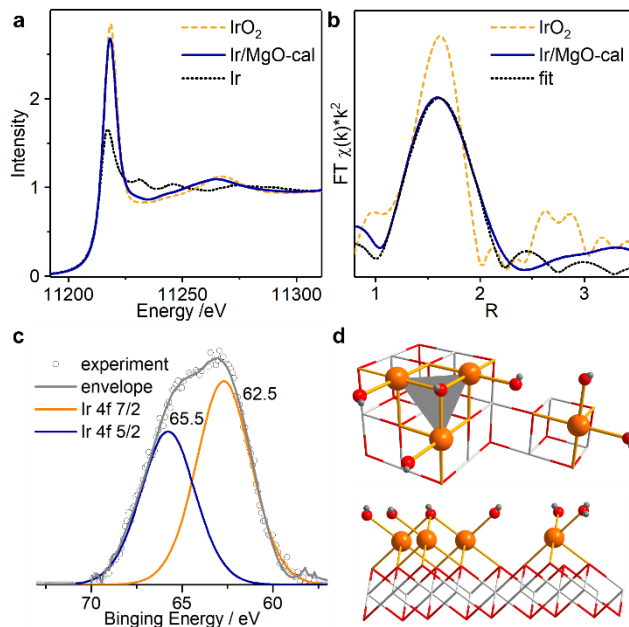
109

110   **Figure 2. Characterization of Ir/MgO-cal** (a) Ir-LIII edge XANES and (b) FT-EXAFS spectra of 1 wt% Ir/MgO-
111   cal, with bulk Ir and IrO$_2$ as references. (c) 4f XPS spectrum of 1 wt% Ir/MgO-cal. (d) top view and side view
112   of a scheme showing the coordination structures of Ir trimer and monomer on MgO(111). (Atom symbols:
113   white, Mg; red, O; orange, Ir; grey, H).

114   To provide further information on the overall atomic and electronic structure of Ir, XAS of 1 wt% Ir/MgO-
115   cal was performed on the Ir-LIII edge under strict air and moisture free atmosphere. The white line
116   intensity and edge energy [11215.5 eV, determined from the first derivatives of $\mu(E)$] in XANES is slightly
117   lower than that for IrO$_2$ (11215.9 eV), indicating a lower oxidation state of Ir. The similar shape of XANES
118   spectra suggests a similar octahedral coordination structure for the Ir cations (Figure 2a). EXAFS in R space
119   had one major scattering peak at *ca.* 2 Å, corresponding to the first coordination shell of iridium (Ir-O,
120   Figure 2b). No strong Ir-Ir at ~2.7 Å or Ir-O-Ir at ~3.1 Å was found, which is consistent with the presence
121   of highly isolated atoms in the STEM images and excludes the presence of iridium or iridium oxide domains.
122   The best fitting of EXAFS data gave 5.0 ± 0.4 Ir-O coordination number at a distance of 2.02 Å ± 0.01 (Table
123   S2), consistent with Ir(III).[42,43] The observation of a doublet at 65.5 and 62.5 eV associated with Ir 4f 5/2
124   and Ir 4f 7/2 by X-ray photoelectron spectroscopy (XPS) further confirms the oxidation state of +III
125   oxidation of Ir (Figure 2c).[44,45] In addition, the symmetrical shape of this doublet is again in full agreement
126   with highly isolated Ir sites and the absence of conductive bulk iridium (oxide) phase.[46] We thus propose
127   that each Ir(III) cation is anchored by three O_{3c}^{2-} or $-OH_{3c}$ sites on MgO(111), coordinates with a hydroxide

128 ion (to balance the charge) and a water molecule (to complete 5 Ir-O coordination) as shown in Figure 2d.
129 Regarding Ir trimers, they are likely bridged by a μ^3 hydroxide anion. Each Ir coordinates to one terminal
130 hydroxide ion for charge compensation. Another structure of Ir trimers bridged by a μ^3-O^{2-} anion with no
131 terminal hydroxide ion is also possible.

132 Both 1 wt% and 0.1 wt% Ir/MgO-cal were then evaluated in the coupling reaction of benzene and ethylene
133 at 3 bar and 180 °C and compared with Ir(O,O-acac)$_2$(C-acac)(py) and Ir(O,O-acac)$_2$(Ph)(py), which are
134 known homogeneous hydroarylation catalysts.[35] We also prepared 1.6 ± 0.4 nm silica-supported Ir
135 nanoparticles as metallic Ir reference (Figure S10-12).[47] Both Ir/MgO-cal catalysts lead to the formation of
136 styrene as the major product (94% and >99% selectivity for 1 wt% and 0.1 wt% materials, respectively –
137 Table 1, Entries 1-2), sharply contrasting with what is observed for the corresponding homogeneous
138 catalytic systems that yield ethylbenzene (Table 1, Entries 3-4). The absence of conversion of benzene
139 with MgO support alone or silica-supported Ir nanoparticles (Table 1, Entries 5-6) supports that isolated
140 Ir sites on MgO are important for catalyzing this reaction.
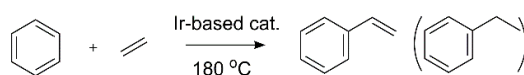
Entry	Catalyst	TON	Product	
			styrene	ethylbenzene
1	1% Ir/MgO-cal	145	94 %	6 %
2	0.1% Ir/MgO-cal	140	>99 %	-
3	Ir(O,O-acac)$_2$(C-acac)(py)	322	-	>99%
4	Ir(O,O-acac)$_2$(Ph)(py)	335	-	>99%
5	Ir/SiO$_2$	< 1	-	-
6	MgO-NS	< 1	-	-
7	0.1% Ir/MgO-NP	110	-	>99%

141 **Table 1. Catalytic activities** Reaction conditions: 5 mL benzene, 3 bar ethylene, react at 180 °C for 3 hours.
142 For entry 1-4 and 7, the mass of Ir of loaded catalysts were kept the same as 1 mg. TON are based on Ir.
143 For entry 5, 200 mg of Ir/SiO$_2$ was loaded.

144 Such an observation highlights that atomically dispersed metal catalysts behave distinctively from their
145 homogeneous counterparts, even though the active metal centers and the surrounding atoms from
146 ligands are the same. To further evaluate the role of the support, we prepared another atomically
147 dispersed Ir catalyst supported on irregular-shaped MgO nanoparticles (MgO-NP) as a reference material
148 (0.1 w% Ir/MgO-NP, Figure S13, 14). However, Ir/MgO-NP only lead to the production of ethylbenzene
149 (Table 1, Entries 7), similarly to the homogenous catalysts but contrary to Ir/MgO-cal. Such a difference in
150 the product is likely due to the special preferential orientation and specific electronic properties of the
151 well-defined MgO(111) support. This polar surface has been proposed to have unique catalytic
152 properties,[48,49] which rises our interests to study the reaction mechanism with combined IR, UV-Vis,
153 isotope labeling and solid-state NMR.

154 To determine whether Ir/MgO-cal catalyzed the reaction through benzene C-H activation, as the same
155 with bis-acac-O,O-Ir(III) complexes (that form phenyl-Ir complexes after reaction),[35] the spent catalyst was
156 analyzed by IR spectroscopy. C-H stretch over 3000 cm^{-1} and C-C stretch in aromatic rings around 1500
157 cm^{-1} proved the generation of phenyl-Ir intermediates (Figure S15), which was also observed on the
158 material pretreated in benzene without ethylene (Figure S16). When C$_6$D$_6$ were used instead, O-D stretch

159 at 2600 cm^{-1} was observed, which might due to the formation of HOD as the result of C-D activation (Figure
160 S16). The generated HOD further protonated MgO support to form -OD groups. To further characterize
161 the adsorbed species, ^{1}H, ^{13}C cross-polarization magic angle spinning (CPMAS) NMR spectra were
162 recorded for Ir/MgO-cal pretreated with ^{13}C-benzene at 180 °C for 3 hours, followed by evacuation under
163 high-vacuum. The ^{13}C solid-state nuclear magnetic resonance (ssNMR) spectrum shows signals at 139 (Ir-
164 C), 127 (*ortho*- and *meta*-C), 118 (*para*-C) ppm as expected for Ir-phenyl species (Figure S17), with similar
165 chemical shifts as compared to these of the Ir(O,O-acac)$_2$(Ph)(py) complex (137, 131, 125, 122 ppm). A
166 signal at 170 ppm is assigned to adsorbed carboxylate species, likely generated from the oxidation of
167 benzene by surface superoxide ions (Figure S18).[50,51] Another evidence of formation of phenyl-Ir
168 intermediates is that the color changed from light yellow to green after treating the catalysts. In fact, UV-
169 Vis diffuse reflectance spectroscopy (DRS) showed a new absorbance band at 680 cm^{-1}, assigned to d-d
170 transition between Ir and phenyl ligands (Figure S19). In contrast, in the absence of atomically dispersed
171 Ir, MgO-NS support alone could not activate benzene to form chemisorbed phenyl moiety (Figure S20),
172 which further supports that C-H bond activation takes place on Ir sites (Figure S21).
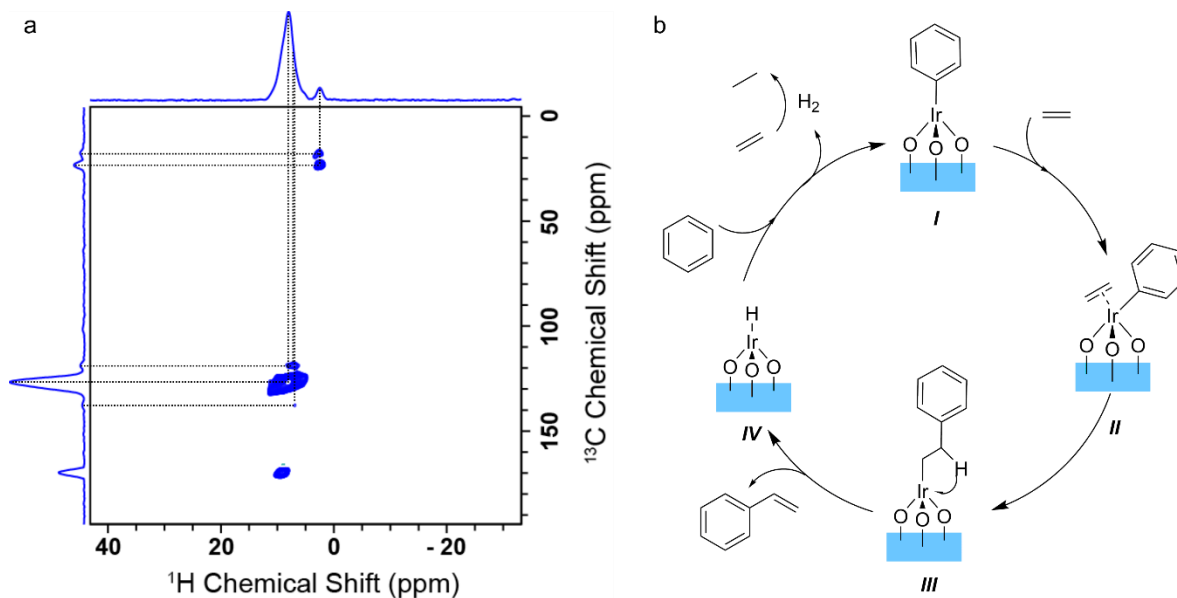

173

174 **Figure 3. Reaction mechanism study.** (a) 2D ^{1}H-^{13}C correlation NMR spectrum of spend Ir/MgO-cal
175 recorded at 400 MHz using a 3.2mm probe and 16kHz MAS. (b) Proposed catalytic cycles of benzene-
176 ethylene coupling towards styrene, the process consists olefin insertion (I to II) and β-hydride elimination
177 (III to IV) along with hydrogenation of ethylene (IV to I).

178 To form styrene, a PhCH$_2$CH$_2$-Ir intermediate is likely also formed via olefin insertion as proposed for the
179 corresponding homogeneous catalysts.[52] The spent catalysts using isotope-labeled reagents (^{13}C-C$_6$H$_6$ +
180 ^{13}C-C$_2$H$_4$) was then characterized utilizing ^{1}H detected 2D ^{1}H-^{13}C correlation Solid-State NMR (Figure 3a).[53]
181 In addition to the set of peaks observed upon reaction of the catalyst with ^{13}C-benzene, new signals appear
182 at 19 (Ir-α-**C**H$_2$) and 24 (β-**C**H$_2$) as well as 129 (phenyl-*C*) ppm, consistent with the proposed PhCH$_2$CH$_2$-Ir
183 intermediate. We propose that this intermediate undergo β-hydride eliminations to generate styrene and
184 a metal hydride intermediate.[54] The production of C$_2$H$_6$ and H$_2$ according to GC analysis is consistent with
185 the formation of these Ir-hydrides (Figure S22); the hydrogenation of ethene to ethane allowing the
186 formation of styrene. We also observe kinetic isotope effect (KIE) upon using D-labeled substrates with

187   secondary KIE's of 1.13 for the reactions carried out with C_6H_6/C_2D_4 vs. C_6H_6/C_2H_4 (Table S3). The value of
188   1.13 obtained from the experiment with deuterated ethylene is consistent with a change of hybridization
189   from sp^3 to sp^2 (1.1 - 1.2)[55] and thereby β-hydride elimination pathway. Based on these experimental
190   results and previous studies on the related homogenous systems, we propose that the catalytic reaction
191   occurs through C-H activation, olefin insertion and β-hydride elimination along with hydrogenation of
192   ethylene as a driving force to release styrene (Figure 3b).

193   In the catalytic benzene-ethylene coupling over 1 wt% Ir/MgO-cal, it is noteworthy to mention that the
194   conversion [turnover number (TON) based on exposed Ir sites] increases linearly and constantly over time
195   for at least 3 hours (Table S4, Figure S23), as expected for a stable catalytic system. We thus characterized
196   the spent catalysts using combined XAS, XPS and ADF-STEM. Both Ir L-III edge XAS (11215.7 eV) and Ir 4f
197   XPS (65.8 and 62.8 eV) showed that Ir species retained their +III oxidation state (Figure S24).

198   The Ir atoms remain highly dispersed as evidenced in ADF-STEM images (Figure 4, Figure S25): although
199   the number of monomers decreased from 86 % to 68 %, no Ir nanoparticles were formed. For the low
200   loading catalysts (0.1 wt% Ir/MgO-cal), the atomic dispersion of Ir is fully maintained despite the high
201   reaction temperature and reductive atmosphere (Figure S26), although the MgO 2D nanosheets breaks
202   into smaller units. The linear TON-time plot and the same turnover frequencies (TOFs) for both catalysts
203   indicate that Ir atoms have likely similar reactivity regardless of their nuclearity as monomers, dimers and
204   trimer. In fact, Ir atoms remain isolated even after treated this material under H_2 at 400 °C for 6 h
205   reduction (Figure S27). Such a high stability is attributed to the strong bonding between Ir cations and the
206   MgO(111) surface. The low-coordinated O_{3c}^{2-} as the only binding sites for Ir on well-defined MgO(111)
207   nanosheets are shown to be strong donor ligands for Ir.
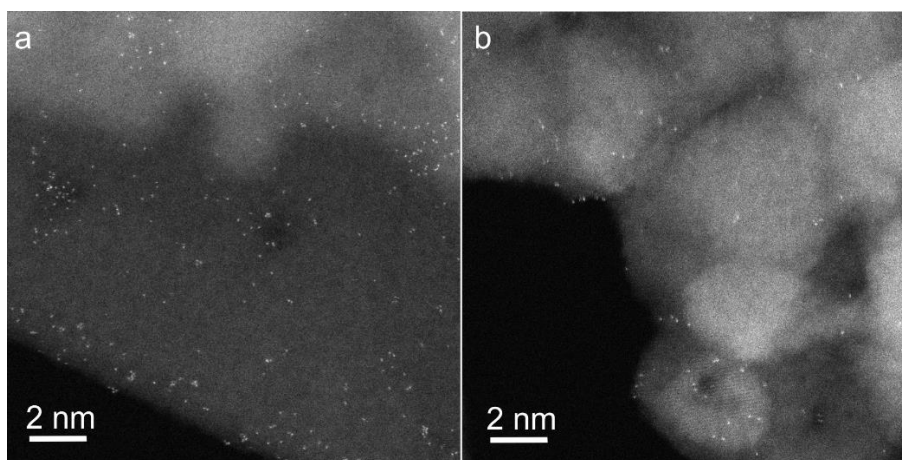
208

209   **Figure 4. Characterization of spent catalysts** Representative ADF-STEM images of spent (a) 1 wt% and (b)
210   0.1 wt% Ir/MgO-cal catalysts.

211   **Conclusion**

212   Using a SOMC approach and well-defined MgO(111) nanosheets, we have prepared atomically dispersed
213   Iridium. At 1 wt% loading, site-isolated monomers and O-bridged Ir dimers and trimers are the major
214   species, while at low loading Ir(III) cations are all monomers with identical coordination structures due to
215   the uniform surface structure of the support. Both catalysts show activity in benzene-ethylene coupling
216   towards styrene, distinct from the behavior of homogeneous catalysts and atomically dispersed Ir on MgO

nanoparticles that lead to production of ethylbenzene. XAS, XPS and ADF-STEM show that the atomically dispersion of Ir species are maintained after catalytic reaction, likely due to the strong ionic interaction between Ir and MgO(111) supports. This study illustrates the power of combined SOMC approach with crystalline 2D supports exposing preferentially one facet to form atomically dispersed catalysts with well-defined coordination structure. This approach will enable a better understanding of their structure-function relationships and offers opportunity, not only to bridge the gap between homogeneous and heterogeneous catalysis but also to uncover new reactions.

Author contribution

P. L. and C. C. conceived the project. C. C. supervised the research; P. L. performed the preparation and most of the characterization and catalytic tests; X. H. performed ADF-STEM measurements; D. M. performed ss-NMR measurements; All authors discussed the results and contributed to the final manuscript.

Author Information

Xing Huang, Current address: College of Chemistry, Fuzhou University, Fuzhou, P. R. China

Competing interests

Authors declare no competing interests.

References

1. Wang, A., Li, J. & Zhang, T. Heterogeneous single-atom catalysis. *Nat. Rev. Chem* **2**, 65-81 (2018).
2. Ji, S. *et al.* Chemical synthesis of single atomic site catalysts. *Chem. Rev.* 10.1021/acs.chemrev.9b00818 (2020).
3. Qiao, B. *et al.* Single-atom catalysis of CO oxidation using Pt_1/FeO_x. *Nat. Chem.* **3**, 634-641 (2011).
4. Malta, G. *et al.* Identification of single-site gold catalysis in acetylene hydrochlorination. *Science* **355**, 1399-1403 (2017).
5. Chen, Z. *et al.* A heterogeneous single-atom palladium catalyst surpassing homogeneous systems for Suzuki coupling. *Nat. Nanotechnol.* **13**, 702-707 (2018).
6. Gu, J., Hsu, C.-S., Bai, L., Chen, H. M. & Hu, X. Atomically dispersed Fe^{3+} sites catalyze efficient CO_2 electroreduction to CO. *Science* **364**, 1091-1094 (2019).

254 7.   Lin, L. *et al.* Low-temperature hydrogen production from water and methanol using Pt/α-MoC
255   catalysts. *Nature* **544**, 80-83 (2017).
256 8.   Jones, J. *et al.* Thermally stable single-atom platinum-on-ceria catalysts via atom trapping. *Science*
257   **353**, 150-154 (2016).
258 9.   Liu, P. *et al.* Photochemical route for synthesizing atomically dispersed palladium catalysts.
259   *Science* **352**, 797-800 (2016).
260 10. Fei, H. *et al.* General synthesis and definitive structural identification of MN_4C_4 single-atom
261   catalysts with tunable electrocatalytic activities. *Nat. Catal.* **1**, 63-72 (2018).
262 11. Liu, D. *et al.* Atomically dispersed platinum supported on curved carbon supports for efficient
263   electrocatalytic hydrogen evolution. *Nat. Energy* **4**, 512-518 (2019).
264 12. Christopher, P. Single-Atom Catalysts: Are All Sites Created Equal? *ACS Energy Lett.* **4**, 2249–2250
265   (2019).
266 13. Liu, P. & Zheng, N. Coordination chemistry of atomically dispersed catalysts. *Natl. Sci. Rev.* **5**, 636-
267   638 (2018).
268 14. Qin, R., Liu, K., Wu, Q. & Zheng, N. Surface coordination chemistry of atomically dispersed metal
269   catalysts. *Chem. Rev.* (2020).
270 15. Parks, G. A. The isoelectric points of solid oxides, solid hydroxides, and aqueous hydroxo complex
271   systems. *Chem. Rev.* **65**, 177-198 (1965).
272 16. Campbell, C. T. & Sauer, J. Introduction: surface chemistry of oxides. *Chem. Rev.* **113**, 3859-3862
273   (2013).
274 17. Hoffman, A. S., Fang, C.-Y. & Gates, B. C. Homogeneity of surface sites in supported single-site
275   metal catalysts: assessment with band widths of metal carbonyl infrared spectra. *J. Phys. Chem.*
276   *Lett* **7**, 3854-3860 (2016).
277 18. DeRita, L. *et al.* Structural evolution of atomically dispersed Pt catalysts dictates reactivity. *Nat.*
278   *Mater.* **18**, 746-751 (2019).
279 19. Fang, C.-Y. *et al.* Reversible metal aggregation and redispersion driven by the catalytic water gas
280   shift half-reactions: interconversion of single-site rhodium complexes and tetrarhodium clusters
281   in zeolite HY. *ACS Catal.* **9**, 3311-3321 (2019).
282 20. Tang, Y. *et al.* Rh single atoms on TiO_2 dynamically respond to reaction conditions by adapting
283   their site. *Nat. Commun* **10**, 1-10 (2019).
284 21. Speck, F. D. *et al.* Atomistic Insights into the Stability of Pt Single-Atom Electrocatalysts. *J. Am.*
285   *Chem. Soc.* **142**, 15496-15504 (2020).
286 22. Ida, S., Kim, N., Ertekin, E., Takenaka, S. & Ishihara, T. Photocatalytic reaction centers in two-
287   dimensional titanium oxide crystals. *J. Am. Chem. Soc.* **137**, 239-244 (2015).
288 23. Zhang, L. *et al.* Graphene defects trap atomic Ni species for hydrogen and oxygen evolution
289   reactions. *Chem* **4**, 285-297 (2018).
290 24. Li, X., Yang, X., Zhang, J., Huang, Y. & Liu, B. In situ/operando techniques for characterization of
291   single-atom catalysts. *ACS Catal.* **9**, 2521-2531 (2019).
292 25. Cui, X., Li, W., Ryabchuk, P., Junge, K. & Beller, M. Bridging homogeneous and heterogeneous
293   catalysis by heterogeneous single-metal-site catalysts. *Nat. Catal.* **1**, 385-397 (2018).
294 26. Gates, B. C., Flytzani-Stephanopoulos, M., Dixon, D. A. & Katz, A. Atomically dispersed supported
295   metal catalysts: perspectives and suggestions for future research. *Catal. Sci. Technol.* **7**, 4259-
296   4275 (2017).
297 27. Liu, P., Abdala, P. M., Goubert, G., Willinger, M.-G. & Copéret, C. Ultrathin Single-crystalline MgO
298   (111) Nanosheets. *Angew. Chem. Int. Ed.* DOI: 10.1002/anie.202013196 (2020).
299 28. Copéret, C. Single-sites and nanoparticles at tailored interfaces prepared via surface
300   organometallic chemistry from thermolytic molecular precursors. *Acc. Chem. Res.* **52**, 1697-1708
301   (2019).

302   29.   Samantaray, M. K. *et al.* The Comparison between Single Atom Catalysis and Surface
303   Organometallic Catalysis. *Chem. Rev.* **120**, 734-813 (2019).
304   30.   Wegener, S. L., Marks, T. J. & Stair, P. C. Design strategies for the molecular level synthesis of
305   supported catalysts. *Acc. Chem. Res.* **45**, 206-214 (2012).
306   31.   Arndtsen, B. A. & Bergman, R. G. Unusually mild and selective hydrocarbon C-H bond activation
307   with positively charged iridium (III) complexes. *Science* **270**, 1970-1973 (1995).
308   32.   Reyes, R. L. *et al.* Asymmetric remote C-H borylation of aliphatic amides and esters with a modular
309   iridium catalyst. *Science* **369**, 970-974 (2020).
310   33.   Dong, Z., Ren, Z., Thompson, S. J., Xu, Y. & Dong, G. Transition-metal-catalyzed C-H alkylation using
311   alkenes. *Chem. Rev.* **117**, 9333-9403 (2017).
312   34.   Cooper, P., Crisenza, G. E., Feron, L. J. & Bower, J. F. Iridium-Catalyzed α-Selective Arylation of
313   Styrenes by Dual C-H Functionalization. *Angew. Chem.* **130**, 14394-14398 (2018).
314   35.   Periana, R. A., Liu, X. Y. & Bhalla, G. Novel bis-acac-O, O-Ir (III) catalyst for anti-Markovnikov,
315   hydroarylation of olefins operates by arene C-H activation. *Chem. Commun.*, 3000-3001 (2002).
316   36.   Hoffman, A. S. *et al.* Beating Heterogeneity of Single-Site Catalysts: MgO-Supported Iridium
317   Complexes. *ACS Catal.* **8**, 3489-3498 (2018).
318   37.   Kawi, S. & Gates, B. C. Organometallic chemistry on the basic magnesium oxide surface: formation
319   of $[HIr_4(CO)_{11}]^-$,$[Ir_6(CO)_{15}]^{2-}$, and $[Ir_8(CO)_{22}]^{2-}$. *Inorg. Chem.* **31**, 2939-2947 (1992).
320   38.   Yang, D. *et al.* Synthesis and characterization of tetrairidium clusters in the metal organic
321   framework UiO-67: Catalyst for ethylene hydrogenation. *J. Catal.* **382**, 165-172 (2020).
322   39.   Frank, M., Kühnemuth, R., Bäumer, M. & Freund, H.-J. Vibrational spectroscopy of CO adsorbed
323   on supported ultra-small transition metal particles and single metal atoms. *Surf. Sci.* **454**, 968-973
324   (2000).
325   40.   Fu, S. L. & Lunsford, J. H. Chemistry of organochromium complexes on inorganic oxide supports.
326   2. The interactions of carbon oxides with chromocene on silica catalysts. *Langmuir* **6**, 1784-1792
327   (1990).
328   41.   Zuo, J.-M., O'keeffe, M., Rez, P. & Spence, J. Charge density of MgO: implications of precise new
329   measurements for theory. *Phys. Rev. Lett.* **78**, 4777 (1997).
330   42.   Lebedev, D. *et al.* Atomically Dispersed Iridium on Indium Tin Oxide Efficiently Catalyzes Water
331   Oxidation. *ACS Cent. Sci.* **6**, 1189-1198 (2020).
332   43.   Shao, X. *et al.* Iridium single-atom catalyst performing a quasi-homogeneous hydrogenation
333   transformation of CO2 to formate. *Chem* **5**, 693-705 (2019).
334   44.   Abbott, D. F. *et al.* Iridium oxide for the oxygen evolution reaction: correlation between particle
335   size, morphology, and the surface hydroxo layer from operando XAS. *Chem. Mater.* **28**, 6591-6604
336   (2016).
337   45.   Pfeifer, V. *et al.* The electronic structure of iridium and its oxides. *Surf. Interface Anal.* **48**, 261-273
338   (2016).
339   46.   Freakley, S. J., Ruiz‐Esquius, J. & Morgan, D. J. The X‐ray photoelectron spectra of Ir, IrO_2 and $IrCl_3$
340   revisited. *Surf. Interface Anal.* **49**, 794-799 (2017).
341   47.   Héroguel, F. *et al.* Dense and narrowly distributed silica-supported rhodium and iridium
342   nanoparticles: Preparation via surface organometallic chemistry and chemisorption stoichiometry.
343   *J. Catal.* **316**, 260-269 (2014).
344   48.   Wu, S. *et al.* Removal of Hydrogen Poisoning by Electrostatically Polar MgO Support for Low-
345   Pressure NH_3 Synthesis at a High Rate over the Ru Catalyst. *ACS Catal.* **10**, 5614-5622 (2020).
346   49.   Noguera, C. Polar oxide surfaces. *J. Phys.: Condens. Matter* **12**, R367-R410 (2000).
347   50.   Anpo, M. *et al.* Generation of superoxide ions at oxide surfaces. *Top. Catal.* **8**, 189 (1999).
348   51.   Sánchez, N. M. & de Klerk, A. Autoxidation of aromatics. *Appl. Petrochem. Res.* **8**, 55-78 (2018).

349   52.   Oxgaard, J., Muller, R. P., Goddard, W. A. & Periana, R. A. Mechanism of homogeneous Ir (III)
350   catalyzed regioselective arylation of olefins. *J. Am. Chem. Soc.* **126**, 352-363 (2004).
351   53.   Mance, D., Comas-Vives, A. & Copéret, C. Proton-Detected Multidimensional Solid-State NMR
352   Enables Precise Characterization of Vanadium Surface Species at Natural Abundance. *J. Phys.*
353   *Chem. Lett* **10**, 7898-7904 (2019).
354   54.   McKeown, B. A. *et al.* Platinum (II)-catalyzed ethylene hydrophenylation: Switching selectivity
355   between alkyl-and vinylbenzene production. *Organometallics* **32**, 2857-2865 (2013).
356   55.   Lee, I. Secondary kinetic isotope effects involving deuterated nucleophiles. *Chem. Soc. Rev.* **24**,
357   223-229 (1995).

358